JOURNAL OF THERMOPHYSICS AND HEAT TRANSFER
Vol. 21, No. 4, October–December 2007

Combining Static and Rotating Magnetic Fields During Modified Vertical Bridgman Crystal Growth

X. Wang*
Scroll Labs, Inc., Bolingbrook, Illinois 60440
N. Ma†
North Carolina State University, Raleigh, North Carolina 27695
D. F. Bliss‡
U. S. Air Force Research Laboratory, Hanscom AFB, Massachusetts 01731
G. W. Iseler§
Iseler Associates, Chelmsford, Massachusetts 01824
and
P. Becla¶
Solid State Scientific, Hollis, New Hampshire 03049

DOI: 10.2514/1.28772

Static magnetic fields have been widely used to control the heat and mass transfer during crystal growth, whereas rotating magnetic fields are attracting a growing attention for crystal-growth technologies from the melt. A combination of static and rotating magnetic fields can be used to control the transport phenomena during semiconductor crystal growth. This paper treats the flow of molten gallium–antimonide and the dopant transport during the vertical Bridgman process using submerged heater growth in this combination of externally applied fields. This paper investigates the effects of these fields on the transport in the melt and on the dopant distributions in the crystal.

Nomenclature

a_1, a_2	=	constants in velocity profile for the axial gap flow
B_{st}	=	flux density of the static magnetic field
B_{rot}	=	flux density of the rotating magnetic field
B_ω	=	amplitude of flux density of the rotating magnetic field
b	=	dimensionless depth of the lower melt
C	=	dimensionless concentration of the dopant in the melt
C_s	=	dimensionless concentration of the dopant in the crystal
c_p	=	specific heat of the melt
D	=	diffusion coefficient for the dopant in the molten semiconductor
f	=	frequency of the alternating current power source
g	=	gravitational acceleration
Ha	=	Hartmann number
h	=	dimensionless length of the entire crystal
$\boldsymbol{j}^*_{\mathrm{st}}$	=	electric current density induced by the static magnetic field
$\boldsymbol{j}^*_{\mathrm{rot}}$	=	electric current density induced by the rotating magnetic field
k	=	thermal conductivity of the melt
k_s	=	segregation coefficient for selenium in gallium–antimonide
m	=	number of pairs of magnet poles
$\hat{\boldsymbol{n}}$	=	outward unit normal vector
Pe_g	=	growth Péclet number
Pe_m	=	species transport Péclet number
Pr	=	Prandtl number
p	=	dimensionless pressure
R	=	crystal's radius or the inner radius of the crucible
Ra	=	Rayleigh number
Re_ω	=	magnetic Reynolds number
r	=	dimensionless radial coordinate in the melt
$\hat{\boldsymbol{r}}$	=	unit vector in the radial direction for the cylindrical coordinate system
$\boldsymbol{S}^*$	=	body force per unit volume produced by the externally applied fields
$\boldsymbol{S}_{\mathrm{st}}$	=	dimensionless body force per unit volume produced by the static magnetic field alone
$\boldsymbol{S}_{\mathrm{rot}}$	=	dimensionless body force per unit volume produced by the rotating magnetic field alone
$S_{\mathrm{rot},r}$	=	radial component of dimensionless body force produced by the rotating magnetic field
$S_{\mathrm{rot},\theta}$	=	azimuthal component of dimensionless body force produced by the rotating magnetic field
$S_{\mathrm{rot},z}$	=	axial component of dimensionless body force produced by the rotating magnetic field
T	=	dimensionless temperature in the melt
T^*_h	=	uniform and constant temperature along the top of the lower melt
T_m	=	magnetic Taylor number
T^*_s	=	solidification temperature of pure gallium–antimonide
t	=	dimensionless time
U_c	=	characteristic velocity in the melt
U_g	=	growth rate or velocity of the crystal-melt interface
$\boldsymbol{v}$	=	dimensionless velocity in the melt
v_r	=	dimensionless radial velocity in the melt
v_θ	=	dimensionless azimuthal velocity in the melt
v_z	=	dimensionless axial velocity in the melt
$\hat{\boldsymbol{x}}$, $\hat{\boldsymbol{y}}$	=	unit vectors for the Cartesian coordinate system
z	=	dimensionless axial coordinate in the melt

Received 8 November 2006; revision received 18 March 2007; accepted for publication 4 April 2007.

*Research Engineer, 479 Quadrangle Drive, Unit G.
†Assistant Professor of Mechanical and Aerospace Engineering, Department of Mechanical and Aerospace Engineering, Campus Box 7910; nancy_ma@ncsu.edu. AIAA Senior Member.
‡Physicist, U.S. Air Force Research Laboratory/SNHC (Optoelectronic Technology Branch), 80 Scott Road.
§Physicist, 26 State Street, Chelmsford, MA.
¶Physicist, 27-2 Wright Road, Hollis, NH.

$\hat{z}$ = unit vector in the axial direction for both the cylindrical and Cartesian coordinate systems
α = dimensionless growth rate or velocity of the crystal-melt interface
β = thermal coefficient of volumetric expansion
Γ = difference between the dopant concentration at the periphery and at the centerline for the crystal which solidified after steady-state transport has been achieved
γ_h = dimensionless radius of the submerged fused-silica heater housing
(ΔT) = difference between the heater's surface temperature and the solidification temperature of pure gallium–antimonide
ζ = dimensionless rescaled axial coordinate in the melt
θ = dimensionless azimuthal coordinate in the melt
$\hat{\boldsymbol{\theta}}$ = unit vector in the azimuthal direction for the cylindrical coordinate system
κ = thermal diffusivity of the melt
μ = dynamic viscosity of the melt
ν = kinematic viscosity of the melt
π = 3.14159 radians
ρ = density of the melt
σ = electrical conductivity of the melt
ϕ = dimensionless electric potential
ϕ_1, ϕ_2 = steady, axisymmetric part of the dimensionless electric potential
ψ = dimensionless Stokes stream function in the melt
ω = circular frequency of the alternating current power source

I. Introduction

A STATIC magnetic field can be used to create a body force which provides an electromagnetic (EM) damping of the melt motion and to eliminate oscillations in the convective transport and thus in the dopant concentration of the crystal. If the magnetic field was strong enough to totally suppress the melt motion, then the dopant transport would be dominated by diffusion and the crystal would solidify with both radial and axial dopant uniformity. Here, a dopant is an element added to give the semiconductor crystal specific electrical and optical properties.To achieve such growth conditions, the species transport Péclet number Pe_m must be small; Pe_m is inversely proportional to the diffusion coefficient for the dopant in the molten semiconductor D. Because typical values [1] of D are 1 to 2×10^{-8} m^2/s, Pe_m is never small for any practical crystal-growth system. Applying a static magnetic field during growth can provide an electromagnetic damping of the melt motion and provide a means to reduce the convective dopant transport and increase the relative importance of diffusion. A crystal grown in static magnetic flux densities ranging from 0.1 to 4 T has significant radial and axial segregations [2,3]. Even in microgravity with a static magnetic field, the convective species transport still plays a strong role and such growth conditions cannot be achieved [4,5]. Therefore, static magnetic fields alone do not seem to be a promising means to control the convective dopant transport to produce a crystal with compositional uniformity. Chedzey and Hurle [6] and Utech and Flemings [7] were the first to demonstrate the benefits of applying static magnetic fields during semiconductor crystal growth. Walker [8] reviewed the literature on the effects of static magnetic fields during crystal growth.

Rotating magnetic fields (RMFs) are widely used in the industrial steel casting process and in metallurgical manufacturing. For the growth of single semiconductor crystals, this technique has attracted rapidly increasing attention in recent years. An RMF is a periodic transverse magnetic field which rotates in the azimuthal direction about the centerline of the melt. An RMF is produced by a number of magnet poles which are placed at equally spaced azimuthal positions around the crystal-growth furnace and which are connected to successive phases of a multiphase ac power source. To date, some numerical and experimental studies have investigated effects of an RMF with two magnet poles on the melt motion [9–17]. In a previous study [18], we demonstrated that an RMF can be used to control the melt motion and species transport during crystal growth, and found that the crystal's radial segregation decreases with the increase of the strength of the RMF. Mullin and Hulme [19] were the first to apply an RMF to semiconductor crystal growth. Currently, rotating magnetic field strengths ranging from 1 to 14 mT are being applied during crystal growth [9,14,20]. Dold and Benz [20] and Gelfgat et al. [21] reviewed the literature on the effects of RMFs on the hydrodynamics and heat transfer during crystal growth.

To minimize the segregation in the crystal, a combination of static and rotating magnetic fields can be applied during growth. Cröll et al. [22] experimentally investigated the influence of static and rotating magnetic fields on heat and mass transfer in silicon floating zones and concluded that the segregation can be strongly influenced by this combination of external magnetic fields. Grants and Gerbeth [23] conducted linear and nonlinear instability analysis in a cylinder with static and rotating magnetic fields. Mößner and Gerbeth [24] quantified the stability threshold for a combination of static and rotating magnetic fields in a cylindrical ampoule.

Semiconductor crystals can be solidified from the melt by the vertical Bridgman process. Ostrogorsky [25] introduced a modification of this method in which a submerged heater separates the melt into two zones, namely, a lower melt and an upper melt. As crystal growth progresses, the crystal solidifies and the crucible is slowly lowered to maintain a constant lower melt depth. The lower melt is continuously replenished with liquid from the upper melt with a composition chosen to offset the increasing dopant level in the lower melt due to rejection at the crystal-growth front for dopant with segregation coefficients less than unity. Ma et al. [26] and Wang et al. [27,28] have shown that this replenishment produces crystals with more radial and axial compositional uniformity, whereas Ostrogorsky and Müller [29] have shown that this modified bottom-seeded method produces crystals with much lower defect densities than crystals grown by other methods.

In the present investigation, we numerically model the melt motion and dopant transport during the vertical Bridgman process using a submerged heater with a combination of static and rotating magnetic fields.

II. Melt Motion

This paper treats the unsteady, axisymmetric species transport of selenium in a gallium–antimonide melt during the vertical Bridgman process using a submerged heater with a combination of externally applied static and rotating magnetic fields. Our dimensionless scheme is shown in Fig. 1, in which $\hat{\boldsymbol{r}}$, $\hat{\boldsymbol{\theta}}$, and $\hat{\boldsymbol{z}}$ are the unit vectors for the cylindrical coordinate system. The coordinates and lengths are normalized by the crystal's radius R, so that r is the dimensionless radial position, θ is the azimuthal position, z is the dimensionless axial position, b is the dimensionless depth of the lower melt, and γ_h is the dimensionless radius of the submerged heater.

The electric current in the melt produces an induced magnetic field which is superimposed upon the externally applied magnetic fields. For all practical crystal-growth processes, the additional magnetic fields produced by the electric currents in the melt are negligible.

The EM body force per unit volume $\boldsymbol{S}^*$ created by the externally applied static and rotating magnetic fields is

$$\boldsymbol{S}^* = (\boldsymbol{j}^*_{\mathrm{st}} \times B_{\mathrm{st}}\hat{\boldsymbol{z}}) + (\boldsymbol{j}^*_{\mathrm{rot}} \times B_{\mathrm{rot}}\hat{\boldsymbol{x}}) + (\boldsymbol{j}^*_{\mathrm{st}} \times B_{\mathrm{rot}}\hat{\boldsymbol{x}}) + (\boldsymbol{j}^*_{\mathrm{rot}} \times B_{\mathrm{st}}\hat{\boldsymbol{z}}) \tag{1}$$

where B_{st} is the flux density of static axial magnetic field, B_{rot} is the flux density of the transverse rotating magnetic field, $\boldsymbol{j}^*_{\mathrm{st}}$ is the electric current density induced by the static magnetic field, and $\boldsymbol{j}^*_{\mathrm{rot}}$ is the electric current density induced by the rotating magnetic field. The electric current densities are generated by the static electric field and induced electric field as given by Ohm's law. Here, $\hat{\boldsymbol{x}}$, $\hat{\boldsymbol{y}}$, and $\hat{\boldsymbol{z}}$ are the unit vectors for the Cartesian coordinate system. In Eq. (1), the last two terms, i.e., the electromagnetic body forces created by $\boldsymbol{j}^*_{\mathrm{st}}$ and the rotating magnetic field and by $\boldsymbol{j}^*_{\mathrm{rot}}$ and the static magnetic field, are

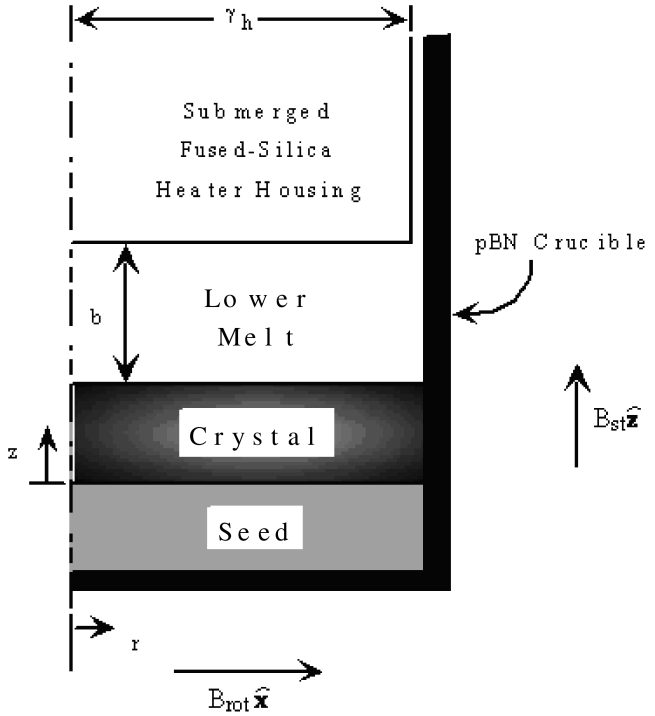

Fig. 1 Vertical Bridgman process using submerged heater growth with an axial static magnetic field and a periodic transverse magnetic field.

negligible compared with the first two terms [24]. In the present study, we neglect these two terms.

An externally applied RMF is given by

$$B_{\text{rot}}\hat{\boldsymbol{x}} = B_\omega r^{m-1}\{\cos[m(\theta-\omega t)]\hat{\boldsymbol{r}} - \sin[m(\theta-\omega t)]\hat{\boldsymbol{\theta}}\} \tag{2}$$

where B_ω is the amplitude of the flux density of the rotating magnetic field, m is the number of pairs of magnet poles, ω is the circular frequency of the ac electric power source, and t is time normalized by R/U_c. Here, $U_c = \mu/\rho R$ is the characteristic velocity where μ is the melt's dynamic viscosity, and ρ is the melt's uniform density.

For the present axisymmetric problem with electrically insulating boundaries, there is no electric potential in the melt due to the static magnetic field. Therefore, the electric potential normalized by $\omega R^2 B_\omega/m$, is produced by the RMF and can be separated into two parts [24]

$$\phi(r,\theta,\zeta,t) = \phi_1(r,\zeta)\cos[m(\theta-\omega t)] + \phi_2(r,\zeta)\sin[m(\theta-\omega t)] \tag{3}$$

Here, $\zeta = -1 + 2(z-\alpha t)/b$ is a rescaled axial coordinate so that $-1 \le \zeta \le +1$. The dimensionless growth rate is $\alpha = U_g/U_c$ where U_g is the growth rate.

An RMF actually produces a periodic, nonaxisymmetric electromagnetic body force in addition to the steady, axisymmetric, azimuthal body force. The frequency of the nonaxisymmetric part of the body force is $2mf$, where f is the frequency of the ac electric power source, and the fluid cannot respond to the nonaxisymmetric part of the electromagnetic body force with such a high frequency. Witkowski and Walker [10] proved that the melt motion driven by the nonaxisymmetric part of the EM body force is negligible, and so we restrict our analysis to the steady electromagnetic body force.

The equations governing the melt motion are

$$(\boldsymbol{v}\cdot\nabla)\boldsymbol{v} = -\nabla p + Ha^2\boldsymbol{S}_{\text{st}} + T_m\boldsymbol{S}_{\text{rot}} + \frac{Ra}{Pr}T\hat{\boldsymbol{z}} + \nabla^2\boldsymbol{v} \tag{4a}$$

$$\nabla\cdot\boldsymbol{v} = 0 \tag{4b}$$

$$(\boldsymbol{v}\cdot\nabla)T = \frac{1}{Pr}\nabla^2 T \tag{4c}$$

$$\left(\nabla^2 - \frac{m^2}{r^2}\right)\phi_1 = -\frac{2}{b}\frac{r^{m-1}}{Re_\omega}\frac{\partial v_\theta}{\partial\zeta} \tag{4d}$$

$$\left(\nabla^2 - \frac{m^2}{r^2}\right)\phi_2 = \frac{r^{m-1}}{Re_\omega}\left(\frac{2}{b}\frac{\partial v_r}{\partial\zeta} - \frac{\partial v_z}{\partial r}\right) \tag{4e}$$

for $0 \le r \le 1$ and $-1 \le \zeta \le +1$. Equations (4a–4c) are the Navier–Stokes equation with the Boussinesq approximation for the thermal buoyancy force, conservation of mass, and conservation of energy, respectively. The combination of Ohm's law and conservation of electric current define the relationships given by Eqs. (4d) and (4e). The melt velocity $\boldsymbol{v} = v_r\hat{\boldsymbol{r}} + v_\theta\hat{\boldsymbol{\theta}} + v_z\hat{\boldsymbol{z}}$ is normalized by U_c, p is the deviation of the pressure from the hydrostatic pressure normalized by $\mu^2/\rho R^2$, $\boldsymbol{S}_{\text{st}}$ is the EM body force per unit volume produced by the static magnetic field normalized by $\sigma U_c B_{\text{st}}^2$, $\boldsymbol{S}_{\text{rot}}$ is the EM body force per unit volume produced by the rotating magnetic field normalized by $\sigma\omega R B_\omega^2/m$, T is the deviation of the temperature from the solidification temperature T_s^* normalized by $(\Delta T) = (T_h^* - T_s^*)$, and electric potentials ϕ_1 and ϕ_2 are normalized by $\omega R^2 B_\omega/m$. Here, T_h^* is the uniform and constant temperature along the top of the lower melt. In Eq. (4a), Ha^2 is the characteristic ratio of the EM body force produced by the static magnetic field to the inertial force, where $Ha = RB_{\text{st}}(\sigma/\mu)^{1/2}$ is the Hartmann number. The dimensionless numbers are

$$T_m = \frac{\sigma\omega B_\omega^2 R^4}{m\rho\nu^2} \tag{5a}$$

$$Ra = \frac{g\beta(\Delta T)R^3}{\nu\kappa} \tag{5b}$$

$$Pr = \frac{\nu}{\kappa} \tag{5c}$$

$$Re_\omega = \frac{\omega R^2}{m\nu} \tag{5d}$$

which are the magnetic Taylor number, the Rayleigh number, the Prandtl number, and the magnetic Reynolds number, respectively. Here, $g = 9.81\ \text{m/s}^2$, whereas the kinematic viscosity and thermal diffusivity of the melt are $\nu = \mu/\rho$ and $\kappa = k/\rho c_p$, respectively. The thermal conductivity, the specific heat, the thermal volumetric expansion coefficient, and the electrical conductivity of the melt are k, c_p, β, and σ, respectively. For a sufficiently large value of B_{st} and for practical growth rates, the heat released by the cooling melt is negligible compared with the conductive heat transfer [30]. The characteristic ratio of Joule heating due to the rotating magnetic field to the inertial force, $\sigma\mu^2 R^4 B_\omega^4/k(\Delta T)m^2 Pr$, is equal to $12681.9B_\omega^4/m^2$ and the characteristic ratio of Joule heating due to the steady magnetic field to the inertial force $\sigma\mu^2 B_{\text{st}}^2/k(\Delta T)\rho Pr$ is equal to $0.000221625B_{\text{st}}^2$. For the range of rotating magnetic fields and steady magnetic fields, these two characteristic ratios are much less than one, so that the effects of Joule heating is negligible.

In Eq. (4a), the electromagnetic body forces due to the static and rotating magnetic fields are

$$\boldsymbol{S}_{\text{st}} = -v_r\hat{\mathbf{r}} - v_\theta\hat{\boldsymbol{\theta}} \tag{6a}$$

$$\boldsymbol{S}_{\text{rot}} = \frac{1}{2}r^{m-1}\left\{-\left(\frac{2}{b}\frac{\partial\phi}{\partial\zeta} + \frac{r^{m-1}}{Re_\omega}v_r\right)\hat{\boldsymbol{r}} + \left[r^m - \left(\frac{2}{b}\frac{\partial\phi_1}{\partial\zeta} + \frac{r^{m-1}}{Re_\omega}v_\theta\right)\right]\hat{\boldsymbol{\theta}} + \left(\frac{\partial\phi_2}{\partial r} + \frac{m}{r}\phi_2 + \frac{2r^{m-1}}{Re_\omega}v_z\right)\hat{\boldsymbol{z}}\right\} \tag{6b}$$

The boundary conditions for electric potential are

$$\frac{\partial\phi_1}{\partial r} = 0, \quad \text{at } r = 1, \quad \text{for } -1 \le \zeta \le +1 \tag{7a}$$

$$\frac{2}{b}\frac{\partial \phi_1}{\partial \zeta} = r^m, \quad \text{at } \zeta = \pm 1, \quad \text{for } 0 \le r \le 1 \tag{7b}$$

$$\frac{\partial \phi_2}{\partial r} = -\frac{\alpha}{Re_\omega} r^{m-1}, \quad \text{at } r = 1, \quad \text{for } -1 \le \zeta \le +1 \tag{7c}$$

$$\frac{\partial \phi_2}{\partial \zeta} = 0, \quad \text{at } \zeta = \pm 1, \quad \text{for } 0 \le r \le 1 \tag{7d}$$

The no-slip and no-penetration conditions along the crucible are

$$v_r = v_\theta = 0, \quad \text{at } r = 1, \quad \text{for } -1 \le \zeta \le +1 \tag{8a}$$

$$v_z = -\alpha, \quad \text{at } r = 1, \quad \text{for } -1 \le \zeta \le +1 \tag{8b}$$

The boundary conditions along the crystal-melt interface are

$$v_r = v_\theta = 0, \quad \text{at } \zeta = -1, \quad \text{for } 0 \le r \le 1 \tag{9a}$$

$$v_z = -\alpha, \quad \text{at } \zeta = -1, \quad \text{for } 0 \le r \le 1 \tag{9b}$$

The boundary conditions along the surface of the fused-silica heater are

$$v_r = v_\theta = 0, \quad \text{at } \zeta = +1, \quad \text{for } 0 \le r \le 1 \tag{10a}$$

$$v_z = 0, \quad \text{at } \zeta = +1, \quad \text{for } 0 \le r \le \gamma_h \tag{10b}$$

Assuming that the density of the crystal and melt are the same, the gap between the heater and the crucible replenishes the solidifying melt at a volumetric flow rate $\pi\alpha$, so that we assume a simple velocity profile

$$v_z = \alpha[-1 + a_1(1 - r) + a_2(1 - r^2)], \quad \text{at } \zeta = +1, \quad \text{for } \gamma_h \le r \le 1 \tag{10c}$$

where $a_1 = 3(1 + \gamma_h^2)/(1 - \gamma_h)^3$ and $a_2 = -2(1 + \gamma_h + \gamma_h^2)/(1 - \gamma_h)^3(1 + \gamma_h)$.

The submerged heater above the lower melt and the heaters adjacent to the periphery of the crucible are adjusted throughout growth so that the crystal-melt interface is planar, the submerged heater adjacent to the melt is held at a uniform and constant temperature T_h^*, and the rate of heat transfer from the crucible to the melt is negligible. Therefore, the thermal boundary conditions are

$$\frac{\partial T}{\partial r} = 0, \quad \text{at } r = 1, \quad \text{for } -1 \le \zeta \le +1 \tag{11a}$$

$$T = 0, \quad \text{at } \zeta = -1, \quad \text{for } 0 \le r \le 1 \tag{11b}$$

$$T = 1, \quad \text{at } \zeta = +1, \quad \text{for } 0 \le r \le 1 \tag{11c}$$

Because the boundary along $r = 1$ is adiabatic, the temperature gradient is primarily axial with the hottest melt at the top and the coldest melt along the bottom adjacent to the crystal-melt interface. Future research will include a more complete thermal model which would include effects of any interface deflection.

We introduce a Stokes stream function for the radial and axial velocities in the meridional circulations

$$v_r = \frac{2}{b}\frac{1}{r}\frac{\partial \psi}{\partial \zeta} \tag{12a}$$

$$v_z = -\frac{1}{r}\frac{\partial \psi}{\partial r} \tag{12b}$$

which identically satisfies conservation of mass for our axisymmetric melt motion. For given values of T_m and λ, we solved for ϕ_1, ϕ_2, v_θ, ψ, and T using a Chebyshev spectral collocation method with Gauss–Lobatto collocation points in r and ζ. Because Eqs. (4a) and (4c), are nonlinear, we used a Newton–Raphson iterative method and incrementally increased T_m and λ from zero. After the Newton–Raphson method converged for a given T_m and λ, we used a continuation method to obtain initial guesses for the coefficients in the spectral representations for $(T_m + \Delta T_m)$ and $(\lambda + \Delta\lambda)$. For values of T_m and λ, the numbers of collocation points were varied to ensure that the results were independent of this number and to ensure that all boundary layers were adequately resolved. For example, for $B_\omega = 10$ mT and $B_{st} = 0$ T, we used 61 collocation points in the radial direction and 41 collocation points in the axial direction. Further increasing these numbers did not change the results. When we doubled the collocation points in the radial direction, the minimum and maximum values of the stream function changed by 0.01%. When we doubled the collocation points in the axial direction, the minimum and maximum values of the stream function changed by 0.012%.

III. Dopant Transport

Before solidification begins, the dopant concentration is uniform, and this initial value is used to normalize the concentration C, so that $C(r, \zeta, t = 0) = 1$. The equation governing the dopant transport is

$$\frac{\partial C}{\partial t} + \boldsymbol{v} \cdot \nabla C = Pe_m^{-1} \nabla^2 C \tag{13}$$

where $Pe_m = U_c R/D$ is the species Péclet number. The boundary condition along the crystal-melt interface is

$$\frac{2}{b}\frac{\partial C}{\partial \zeta} = Pe_g(k_s - 1)C, \quad \text{at } \zeta = -1, \quad \text{for } 0 \le r \le 1 \tag{14}$$

where $Pe_g = U_g R/D = \alpha Pe_m$ is the growth Péclet number and k_s is the segregation coefficient for the dopant in the molten semiconductor. For selenium in molten gallium–antimonide, $k_s = 0.1$, so that the crystal rejects selenium into the melt along the crystal-melt interface. To compensate for this elevated level of dopant, the melt is replenished with dopant-depleted melt, so that the boundary condition along the gap between the heater and the crucible is

$$C = k_s, \quad \text{at } \zeta = 1, \quad \text{for } \gamma_h \le r \le 1 \tag{15}$$

The boundary conditions along the impermeable surfaces of the crucible and fused-silica heater are $\hat{\boldsymbol{n}} \cdot \nabla C = 0$, where $\hat{\boldsymbol{n}}$ is the outward unit normal vector.

Assuming that the dopant does not diffuse in the solid crystal and that the density of the solid and liquid are the same, the concentration in the crystal $C_s(r, z)$, normalized by the initially uniform dopant concentration in the melt, is $C_s(r, z) = k_s C(r, \zeta = -1, t = z/\alpha)$. The first-grown part of the crystal solidifies at $t = 0$ with $C_s(r, 0) = k_s$.

We use a Chebyshev spectral collocation method with a second-order implicit time integration scheme to solve Eq. (13) with Gauss–Lobatto collocation points in r and ζ. We use a sufficient number of collocation points to resolve the concentration gradients near the boundaries. We integrate from $t = 0$ to a t which is slightly less than h/α, where h is the dimensionless length of the entire crystal. We use a large enough number of time steps such that the results do not change by increasing the number of time steps. For example, for $B_\omega = 10$ mT and $B_{st} = 0$ T, we used 61 collocation points in the radial direction, 41 collocation points in the axial direction and 10,000 time steps. Further increasing these numbers did not change the results. When we increased the number of collocation points in radial direction to 121, the maximum value of the concentration at

$t = 0.0883$ changed by 0.0022%. When we increased the number of collocation points in axial direction to 81, the maximum value of concentration at $t = 0.0883$ changed by less than 0.0001%. When we increased the number of time steps to 14,000, the maximum value of concentration at $t = 0.0883$ changed by 0.014%.

IV. Results

For the experimental configuration at the U.S. Air Force Research Laboratory, the RMF has $m = 3$ pole pairs and a frequency $f = 60$ Hz, for which $\omega = 2\pi f = 376.99$ rad/s. For a typical process with selenium-doped gallium–antimonide, $(\Delta T) = 20$ K, $U_g = 2$ mm/h or 0.5556 μm/s, $U_c = 15.3234$ μm/s, for which $\alpha = 0.03626$, $Pe_m = 19.15$, $Pe_g = 0.6944$, $Ra = 88,672$, and $Ra = 205,020$. Under these conditions, $Ha = 1.6449 B_{\mathrm{st}}$ and $T_m = 1.849 \times 10^{10} B_\omega^2$ with B_{st} and B_ω in Tesla. For $h = 3.2$, the dimensionless time to grow the crystal is $h/\alpha = 88.26$.

With neither a static nor a rotating magnetic field, the driving mechanisms for the melt motion are the gap flow and the crystal-growth flow. This flow produces a meridional melt motion in which the replenished fluid enters the lower melt from the gap, flows axially downward and radially inward, and then solidifies along the crystal-melt interface at $\zeta = -1$. The maximum magnitude of the velocity is equal to the dimensionless growth rate α, and the maximum value of the meridional stream function is half of this value, $\psi_{\max} = 0.01813$. When the crystal begins to solidify, dopant is rejected along the crystal-melt interface. This rejection causes the concentration in the melt to rise above the initial uniform concentration $C = 1$. The minimum value of the concentration is always 0.1 because the melt is replenished with dopant-depleted fluid having concentration $C = k_s = 0.1$ adjacent to $r = 1$ and $\zeta = +1$. The maximum value of the concentration is always at the centerline at the crystal-melt interface at $r = 0$ and $\zeta = -1$. As growth progresses, the dopant diffuses in the melt and the melt motion convects the dopant-depleted fluid axially downward and radially inward, causing the melt to have concentration $C < 1$ everywhere. An objective is to compensate for the elevated level of dopant due to the rejection along the crystal-melt interface. With an initial concentration $C(r, \zeta, t = 0) = 1$ and with replenishment of fluid having $C = 0.1$, $C < 1$ everywhere in the melt after steady state is achieved. Ma et al. [26] found that the dopant transport reaches a steady state when 88% of the crystal has grown, which corresponds to a dimensionless time 77.67. After this time, the melt's concentration distribution does not change, so that the remaining 12% of the crystal solidifies with axial uniformity and the same radial distribution. For this section of the crystal, we characterize the radial segregation after steady-state transport has been achieved by the difference between the crystal's concentration at the centerline and the concentration at the periphery, $\Gamma = C_s(0, 3.192) - C_s(1, 3.192)$. For the present flow, Ma et al. [26] found that $\Gamma = 0.004579$.

A rotating magnetic field generates an EM body force that drives an azimuthal melt motion, which in turn induces a meridional melt motion. We present results without a static magnetic field and with an RMF for $B_\omega = 2$ mT. Figures 2a and 2b present the contours of components of the steady, axisymmetric electric potentials in the melt ϕ_1 and ϕ_2, respectively. The minimum and maximum values of ϕ_1 are -0.1357 and 0.1357, respectively, whereas the minimum and

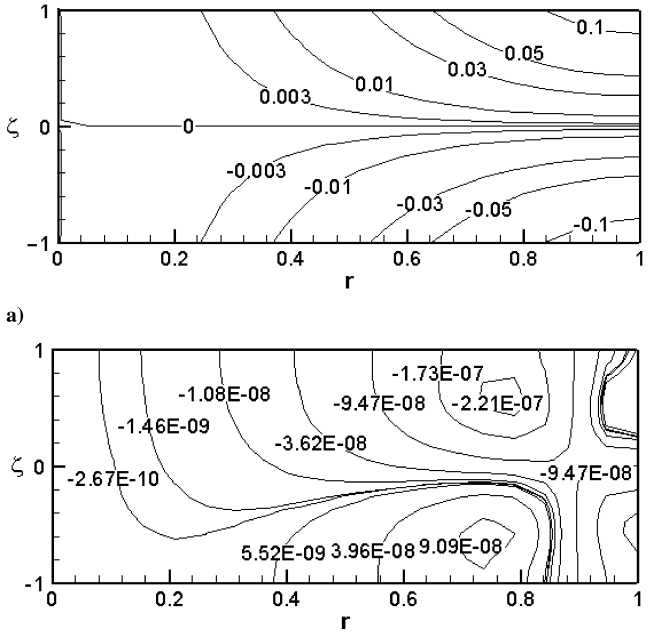

Fig. 2 Components of the electric potential with an RMF alone for $B_\omega = 2$ mT: a) $\phi_1(r, \zeta)$, and b) $\phi_2(r, \zeta)$.

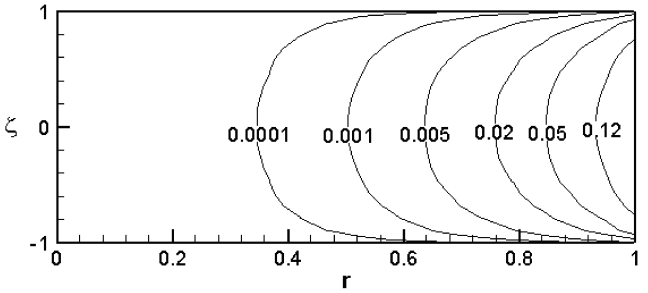

Fig. 3 Azimuthal electromagnetic body force $S_{\mathrm{rot},\theta}(r, \zeta)$ with an RMF alone for $B_\omega = 2$ mT.

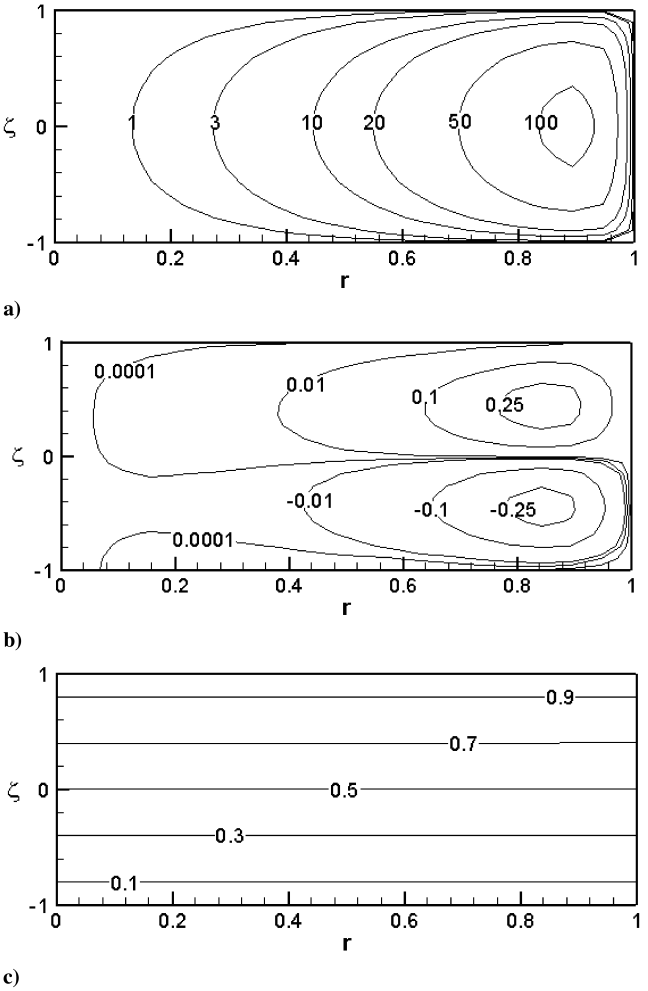

Fig. 4 Melt motion with an RMF alone for $B_\omega = 2$ mT: a) azimuthal velocity $v_\theta(r, \zeta)$, b) meridional stream function $\psi(r, \zeta)$, and c) temperature $T(r, \zeta)$.

maximum values of ϕ_2 are -2.32×10^{-7} and 1.03×10^{-7}, respectively. From Eq. (6b), the radial and axial components of the EM body forces, $S_{\mathrm{rot},r}$ and $S_{\mathrm{rot},z}$, respectively, are driven by ϕ_2, whereas the azimuthal component of the EM body force $S_{\mathrm{rot},\theta}$ is driven by ϕ_1. Because the magnitude of ϕ_1 is six orders of magnitude larger than that of ϕ_2, the azimuthal EM body force is dominant. We present the contours of $S_{\mathrm{rot},\theta}$ in Fig. 3, and its maximum value is 0.2187 at $r = 1$ and $z = 0$. In Fig. 4a, we present the contours of the azimuthal velocity, in which the maximum value is 114.11. In Fig. 4b, we present the contours of the meridional stream function in which the minimum and maximum values are -0.3070 and 0.3295, respectively. The magnitudes of these values are much larger than the $\psi_{\max}$ produced by the gap and crystal-growth flows, so that the flow produced by the RMF has dominated the melt motion. In Fig. 4b, the upper circulation is counterclockwise, whereas the lower circulation is clockwise. The only evidence of the melt motion produced by the gap and crystal-growth flows is in the 0.0001 and 0.01 contours which originate from the gap where the melt is replenished near $r = 1$ and $\zeta = +1$. Figure 4c presents the isotherms in the melt, which indicates that the buoyant convection is negligible. Because the azimuthal body force induces an additional meridional melt motion, there is a stronger convective mixing of the melt, and the dopant transport reaches a steady state at an earlier stage of growth. In Fig. 5a, we present the constant-concentration curves in the melt after the dopant transport has reached a steady state when $t = 22.95$ after 26% of the crystal has grown. The minimum and maximum values of the concentration are 0.1 and 0.1471, respectively. The constant-concentration curves in the crystal are presented in Fig. 5b. After $t = 22.9$, the crystal solidifies with the same radial distribution and $\Gamma = 0.002559$.

Table 1 lists the minimum and maximum values of the components of the electric potential and the values of the components of the EM body force for different flux densities of the rotating magnetic field. When we increase the strength of the RMF, the magnitude of ϕ_1 decreases while the magnitude of ϕ_2 increases. However, ϕ_1 is much larger than ϕ_2, so that the azimuthal component of the EM body force continues to dominate. The meridional melt motion produced by the RMF dominates the other flows. For example, for $B_\omega = 6$ mT, the minimum and maximum values of the stream function are -3.5516 and 3.5844, respectively, and these values are much larger in magnitude than those for $B_\omega = 2$ mT. This much stronger meridional melt motion produces a much stronger convective species transport and thus a crystal with more compositional uniformity in both the radial and axial directions. For $B_\omega = 6$ mT, the dopant transport reaches steady state when 12.5% of the crystal has grown so that 87.5% of the crystal solidifies with the same radial distribution. For this flux density, there is less radial segregation with $\Gamma = 0.001627$. When we further increase the flux density to $B_\omega = 14$ mT, the strength of the flow increases as reflected in the minimum and maximum values of the stream function which are -8.6359 and 8.6712, respectively. The flow induced by the RMF has completely dominated as shown in Fig. 6. This stronger meridional melt motion provides an even stronger convective mixing of the melt so that the concentration in the melt and correspondingly in the crystal become more uniform. For $B_\omega = 14$ mT the dopant transport reaches steady state when 5% of the crystal has grown so that 95% of the crystal solidifies with the same radial distribution. For this flux density, there is even less radial segregation with $\Gamma = 0.001148$. Figure 7 provides the compositional distributions in the crystal after the steady-state transport has been reached, $C(r, z = 3.1997)$, for $B_\omega = 0, 2, 6,$ and 14 mT. In Fig. 7, we include the value for $B_\omega = 0$ mT in which the flow is driven by the gap and crystal-growth flows.

Table 1 Minimum and maximum values of the components of the electric potential and electromagnetic body force

	$B_\omega = 2$ mT	$B_\omega = 6$ mT	$B_\omega = 14$ mT
$\phi_{1,\min}$	-0.1357	-0.1355	-0.1348
$\phi_{1,\max}$	0.1357	0.1355	0.1348
$\phi_{2,\min}$	-2.3291×10^{-7}	-2.0636×10^{-6}	-5.1923×10^{-6}
$\phi_{2,\max}$	1.0258×10^{-7}	1.9142×10^{-6}	5.0345×10^{-6}
$S_{\mathrm{rot},r,\min}$	-8.5824×10^{-6}	-5.9835×10^{-5}	-1.2101×10^{-4}
$S_{\mathrm{rot},r,\max}$	7.0928×10^{-6}	1.2128×10^{-4}	5.0187×10^{-4}
$S_{\mathrm{rot},\theta,\min}$	0	0	0
$S_{\mathrm{rot},\theta,\max}$	0.2187	0.2193	0.2209
$S_{\mathrm{rot},z,\min}$	-1.5279×10^{-5}	-2.0104×10^{-4}	-4.4876×10^{-4}
$S_{\mathrm{rot},z,\max}$	1.5051×10^{-5}	2.0049×10^{-4}	4.4821×10^{-4}

We investigate the effects of a combination of static and rotating magnetic fields on the melt motion and dopant transport. For weak RMFs, when we add a static field $B_{\mathrm{st}} = 0.1$ T, the flow is completely suppressed, and so we only present results for larger RMFs. The static magnetic field provides an EM damping of the meridional flow induced by the RMF. The maximum value of the azimuthal velocity has reduced to 482, which is much smaller than the value of 2234.7 with RMF alone for $B_\omega = 14$ mT. We present the meridional melt motion with $B_\omega = 14$ mT and $B_{\mathrm{st}} = 0.1$ T in Fig. 8. In Fig. 8, the flow near the centerline is significantly damped and the meridional circulations have been reduced to a much smaller volume near the

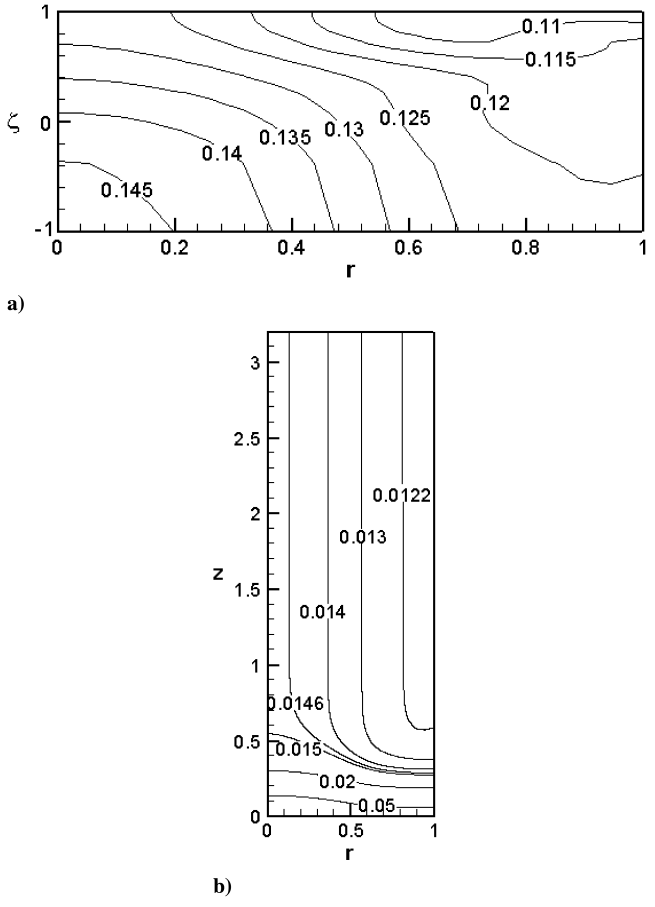

Fig. 5 Constant-concentration curves in the melt and in the crystal with an RMF alone for $B_\omega = 2$ mT: a) $C(r, \zeta, t = 22.95)$, and b) $C_s(r, z)$.

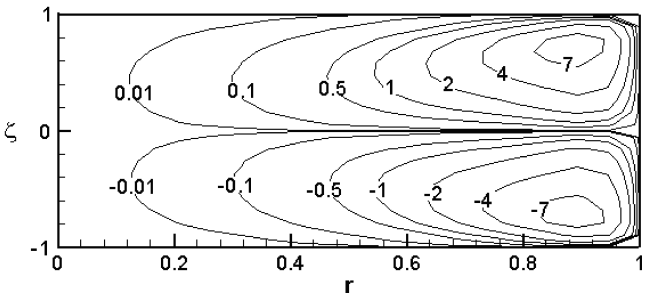

Fig. 6 Meridional stream function $\psi(r, \zeta)$ with an RMF alone for $B_\omega = 14$ mT.

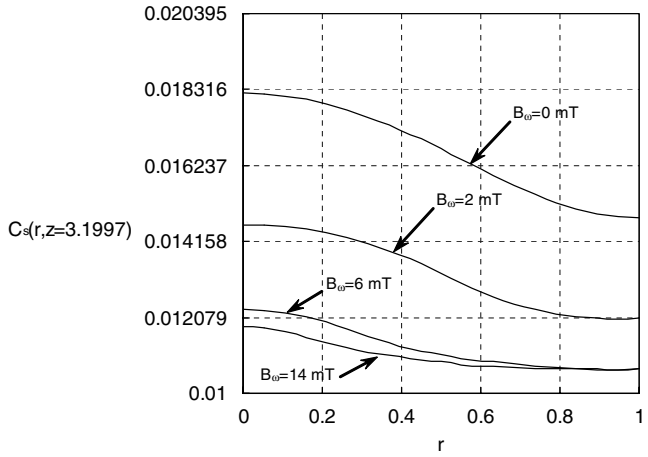

Fig. 7 Radial concentration distributions in the crystal after steady-state transport has been reached with an RMF alone.

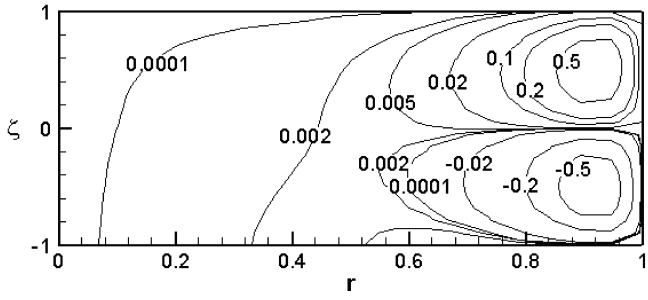

Fig. 8 Meridional stream function $\psi(r, \zeta)$ for $B_\omega = 14$ mT and $B_{st} = 0.1$ T.

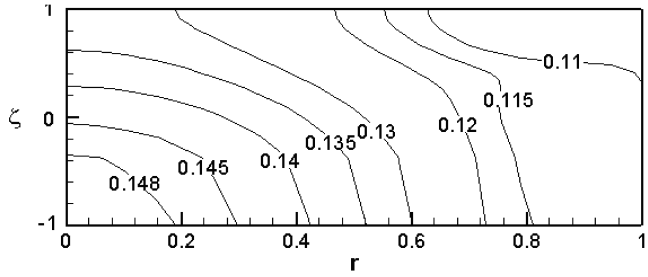

a)

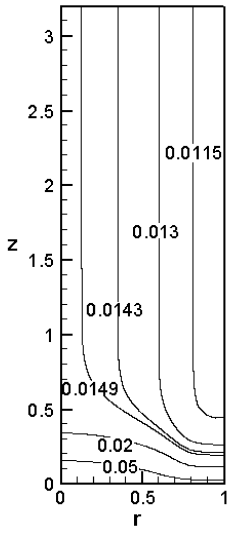

b)

Fig. 9 Constant-concentration curves in the melt and in the crystal for $B_\omega = 14$ mT and $B_{st} = 0.1$ T: a) $C(r, \zeta, t = 23.65)$, and b) $C_s(r, z)$.

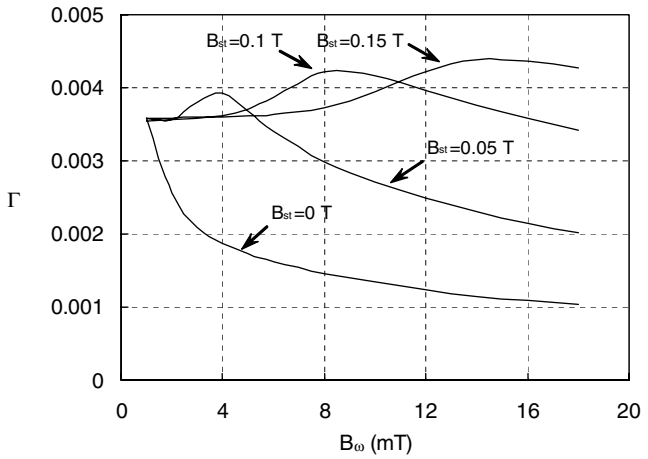

Fig. 10 Radial segregation in the crystal after steady-state transport has been reached for a combination of static and rotating magnetic fields.

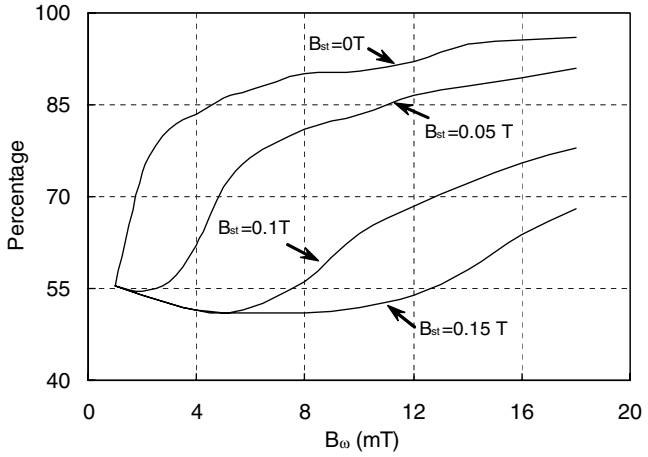

Fig. 11 Percentage of the crystal which has axial compositional uniformity for a combination of static and rotating magnetic fields.

periphery of the crucible. The flow is much weaker, as reflected in the minimum and maximum values of ψ, which are -0.7757 and 0.8002, respectively. The convective dopant transport is correspondingly weaker with a combination of static magnetic and rotating magnetic fields, and the dopant transport reaches a steady state later when 26.8% of the crystal has grown. Figure 9a presents the constant-concentration curves in the melt after steady-state transport has been reached at $t = 23.65$, whereas Fig. 9b presents the constant-concentration curves in the crystal for $B_\omega = 14$ mT and $B_{st} = 0.1$ T. The top 73.2% of the crystal has axial compositional uniformity, and the radial segregation is characterized by $\Gamma = 0.003764$.

Figure 10 presents the value of Γ for several combinations of static and rotating magnetic fields. For a given static magnetic field, increasing the flux density of the RMF initially increases the radial segregation and then decreases the segregation. Figure 11 presents the percentage of the crystal which has axial compositional uniformity for several combinations of static and rotating magnetic fields. For a given static magnetic field, this percentage increases as the flux density of the RMF increases. For a given RMF, the percentage decreases as the flux density of the static magnetic field increases.

V. Conclusions

We have developed a numerical model that can treat the unsteady transport in the melt and predict the dopant transport in the crystal for vertical Bridgman process using submerged heater growth with a combination of static and rotating magnetic fields. We investigated

the effects of these externally applied magnetic fields on the melt motion and dopant transport. With a rotating magnetic field alone, we found that the radial segregation decreases and the percentage of the crystal which solidifies with axial uniformity increases as flux density of the rotating magnetic field increases. With a combination of static and rotating magnetic fields, the static magnetic field damps the stirring driven by the rotating magnetic field. Therefore, for a given rotating magnetic field, the percentage of the crystal which solidifies with axial uniformity decreases as the flux density of the static magnetic field increases.

Acknowledgments

This research was supported by the U.S. Air Force Office of Scientific Research under grant FA9550-04-1-0249. The calculations were performed on the Cray X1 provided by the Department of Defense High Performance Computing Modernization Program under grant AFSNH2487 and on the IBM pSeries 690 provided by the National Computational Science Alliance under grant DMR030015.

References

[1] Khine, Y. Y., Banish, R. M., and Alexander, J. I. D., "Convective Contamination in Self-Diffusivity Experiments with an Applied Magnetic Field," *Journal of Crystal Growth*, Vol. 250, Nos. 1–2, 2003, pp. 274–278.

[2] Wang, X., and Ma, N., "Numerical Model for Bridgman–Stockbarger Crystal Growth with a Magnetic Field," *Journal of Thermophysics and Heat Transfer*, Vol. 19, No. 3, 2005, pp. 406–412.

[3] Ma, N., and Walker, J. S., "Parametric Study of Segregation Effects During Vertical Bridgman Crystal Growth with an Axial Magnetic Field," *Journal of Crystal Growth*, Vol. 208, No. 1, 2000, pp. 757–771.

[4] Ma, N., and Walker, J. S., "Magnetic Damping of Buoyant Convection During Semiconductor Crystal Growth in Microgravity. Continuous Random g-Jitters," *Physics of Fluids*, Vol. 8, Nos. 1–4, 1996, pp. 944–953.

[5] Ma, N., and Walker, J. S., "Magnetic Damping of Buoyant Convection During Semiconductor Crystal Growth with g-Jitters," *Journal of Thermophysics and Heat Transfer*, Vol. 11, No. 2, 1997, pp. 212–215.

[6] Chedzey, H. A., and Hurle, D. T. J., "Avoidance of Growth-Striae in Semiconductor and Metal Crystals Grown by Zone-Melting Techniques," *Nature*, Vol. 210, May 1966, pp. 933–934.

[7] Utech, H. P., and Flemings, M. C., "Elimination of Solute Banding in Indium Antimonide Crystals by Growth in a Magnetic Field," *Journal of Applied Physics*, Vol. 37, No. 7, 1966, pp. 2021–2024.

[8] Walker, J. S., "Models of Melt Motion, Heat Transfer, and Mass Transport During Crystal Growth with Strong Magnetic Fields," *Role of Magnetic Fields in Crystal Growth*, Progress in Crystal Growth and Characterization of Materials, edited by K. W. Benz, Elsevier, Amsterdam, Vol. 38, Nos. 1–4, 1999, pp. 195–213.

[9] Ghaddar, C. K., Lee, C. K., Motakef, S., and Gillis, D. C., "Numerical Simulation of THM Growth of CdTe in Presence of Rotating Magnetic Fields (RMF)," *Journal of Crystal Growth*, Vol. 205, Nos. 1–2, 1999, pp. 97–111.

[10] Witkowski, L. M., and Walker, J. S., "Nonaxisymmetric Flow in a Finite-Length Cylinder with a Rotating Magnetic Field," *Physics of Fluids*, Vol. 11, No. 7, 1999, pp. 1821–1826.

[11] Dold, P., Cröll, A., Lichtensteiger, M., Kaiser, T., and Benz, K. W., "Floating Zone Growth of Silicon in Magnetic Fields 4: Rotating Magnetic Fields," *Journal of Crystal Growth*, Vol. 231, Nos. 1–2, 2001, pp. 95–106.

[12] Salk, M., Fiederle, M., Benz, K. W., Senchenkov, A. S., Egorov, A. V., and Matioukhin, D. G., "CdTe and $CdTe_{0.9}Se_{0.1}$ Crystals Grown by the Travelling Heater Method Using a Rotating Magnetic Field," *Journal of Crystal Growth*, Vol. 138, Nos. 1–4, 1994, pp. 161–167.

[13] Ma, N., Walker, J. S., Lüdge, A., and Riemann, H., "Combining a Rotating Magnetic Field and Crystal Rotation in the Floating-Zone Process with a Needle-Eye Induction Coil," *Journal of Crystal Growth*, Vol. 230, Nos. 1–2, 2001, pp. 118–124.

[14] Wang, X., Ma, N., Bliss, D. F., Iseler, G. W., and Becla, P., "Comparing Modified Vertical Gradient Freezing with Rotating Magnetic Fields or with Steady Magnetic and Electric Fields," *Journal of Crystal Growth*, Vol. 287, No. 2, 2006, pp. 270–274.

[15] Fiederle, M., Eiche, C., Joerger, W., Salk, M., Senchenkov, A. S., Egorov, A. V., Ebling, D. G., and Benz, K. W., "Radiation Detector Properties of $CdTe_{0.9}Se_{0.1}$:Cl Crystals Grown Under Microgravity in a Rotating Magnetic Field," *Journal of Crystal Growth*, Vol. 166, Nos. 1–4, 1996, pp. 256–260.

[16] Volz, M. P., Walker, J. S., Schweizer, M., Cobb, S. S., and Szofran, F. R., "Bridgman Growth of Germanium Crystals in a Rotating Magnetic Field," *Journal of Crystal Growth*, Vol. 282, Nos. 3–4, 2005, pp. 305–312.

[17] Walker, J. S., Volz, M. P., and Mazuruk, K., "Rayleigh–Benard Instability in a Vertical Cylinder with a Rotating Magnetic Field," *International Journal of Heat and Mass Transfer*, Vol. 47, Nos. 8–9, 2004, pp. 1877–1887.

[18] Wang, X., Ma, N., Bliss, D. F., Iseler, G. W., and Becla, P., "Parametric Study of Modified Vertical Bridgman Growth in a Rotating Magnetic Field," *Journal of Thermophysics and Heat Transfer*, Vol. 20, No. 3, 2006, pp. 384–388.

[19] Mullin, J. B., and Hulme, K. F., "Use of Electromagnetic Stirring in Zone Refining," *Journal of Electronics and Control*, Vol. 4, 1958, pp. 170–174.

[20] Dold, P., and Benz, K. W., "Rotating Magnetic Fields: Fluid Flow and Crystal Growth Applications," *Progress in Crystal Growth and Characterization of Materials*, edited by K. W. Benz, Elsevier, Amsterdam, Vol. 38, Nos. 1–4, 1999, pp. 7–38.

[21] Gelfgat, Y. M., Krumin, J., and Abricka, M., "Rotating Magnetic Fields as a Means to Control the Hydrodynamics and Heat Transfer in Single Crystal Growth Processes," *Progress in Crystal Growth and Characterization of Materials*, edited by K. W. Benz, Elsevier, Amsterdam, Vol. 38, Nos. 1–4, 1999, pp. 59–71.

[22] Cröll, A., Dold, P., Kaiser, T., Szofran, F. R., and Benz, K. W., "Influence of Static and Rotating Magnetic Fields on Heat and Mass Transfer in Silicon Floating Zones," *Journal of the Electrochemical Society*, Vol. 146, No. 6, 1999, pp. 2270–2275.

[23] Grants, I., and Gerbeth, G., "Rayleigh–Benard Instability in a Vertical Cylinder Under Influence of Rotating and Steady Magnetic Fields," *Physics of Fluids*, Vol. 16, No. 6, 2004, pp. 2088–2096.

[24] Mößner, R., and Gerbeth, G., "Buoyant Melt Flows Under the Influence of Steady and Rotating Magnetic Fields," *Journal of Crystal Growth*, Vol. 197, Nos. 1–2, 1999, pp. 341–354.

[25] Ostrogorsky, A. G., "Numerical Simulation of Single Crystal Growth by Submerged Heater Method," *Journal of Crystal Growth*, Vol. 104, No. 2, 1990, pp. 233–238.

[26] Ma, N., Bliss, D. F., and Iseler, G. W., "Vertical Gradient Freezing of Doped Gallium–Antimonide Semiconductor Crystals Using Submerged Heater Growth and Electromagnetic Stirring," *Journal of Crystal Growth*, Vol. 259, Nos. 1–2, 2003, pp. 26–35.

[27] Wang, X., Ma, N., Bliss, D. F., and Iseler, G. W., "Semiconductor Crystal Growth by Modified Vertical Gradient Freezing with Electromagnetic Stirring," *Journal of Thermophysics and Heat Transfer*, Vol. 19, No. 1, 2005, pp. 95–100.

[28] Wang, X., Ma, N., Bliss, D. F., and Iseler, G. W., "Solute Segregation During Modified Vertical Gradient Freezing of Alloyed Compound Semiconductor Crystals with Magnetic and Electric Fields," *International Journal of Heat and Mass Transfer*, Vol. 49, Nos. 19–20, 2006, pp. 3429–3438.

[29] Ostrogorsky, A. G., and Müller, G., "Normal and Zone Solidification Using the Submerged Heater Method," *Journal of Crystal Growth*, Vol. 137, Nos. 1–2, 1994, pp. 64–71.

[30] Ma, N., and Walker, J. S., "Model of Dopant Transport During Bridgman Crystal Growth with Magnetically Damped Buoyant Convection," *Journal of Heat Transfer*, Vol. 122, No. 1, 2000, pp. 159–164.